PHYSICS

Demonstration of negative refraction induced by synthetic gauge fields

Yihao Yang[1,2,3]†, Yong Ge[4]†, Rujiang Li[2,3]†, Xiao Lin[1], Ding Jia[4], Yi-jun Guan[4], Shou-qi Yuan[4], Hong-xiang Sun[4]*, Yidong Chong[2,3]*, Baile Zhang[2,3]*

Negative refraction is a counterintuitive wave phenomenon that has inspired the development of metamaterials and metasurfaces with negative refractive indices and surface phase discontinuities, respectively. Recent theories have proposed an alternative mechanism for negative refraction: Synthetic gauge fields, induced by either dynamical modulation or motion, can shift a material's dispersion in momentum space, forcing a positive refractive index medium to exhibit negative refraction above a certain threshold. However, this phenomenon has not previously been observed. Here, we report on the experimental demonstration of gauge field–induced negative refraction in a twisted bilayer acoustic metamaterial. The synthetic gauge fields arise in a projected two-dimensional geometry and can be continuously tuned by varying the wave number along the third dimension. Gauge field–induced waveguiding with backward-propagating modes is also demonstrated in a trilayer configuration. These results introduce a mechanism for performing wave manipulation in artificially engineered materials.

INTRODUCTION

Light, sound, and other waves can change direction when crossing the interface between two media with different refractive indices—the well-known phenomenon of refraction. Typically, the incident and refracted waves lie on opposite sides of the interface normal, a situation referred to as "positive" refraction. The past few decades, however, have witnessed the rise of artificially engineered materials (i.e., metamaterials and metasurfaces) with many capabilities, one of which is the manifestation of "negative" refraction, whereby the refracted wave lies on the same side of the interface normal as the incident wave (*1*–*6*). Negative refraction in metamaterials and metasurface arises from two distinct mechanisms, namely, negative bulk effective refractive indices (for metamaterials) and surface phase discontinuities (for metasurfaces).

The relation between the incident angle and refraction angle can be determined by applying momentum conservation across the interface and analyzing the wave dispersion relations in the media on each side of the interface. Without loss of generality, consider a beam incident from left to right (Fig. 1). A negative refractive index (Fig. 1A) introduces negative dispersion, which reverses the refraction direction from positive to negative, as originally proposed by Veselago (*1*) and subsequently confirmed through numerous experimental and theoretical works (*2*–*5*, *7*, *8*). On the other hand, a surface phase discontinuity (Fig. 1B), which can be accomplished with a metasurface lens, can provide a momentum change Δk along the interface to compensate for the momentum mismatch, hence allowing for negative refraction between two positive refractive index media (*6*, *9*, *10*).

There is a third distinct approach to negative refraction that has recently been proposed (*11*, *12*), which is to shift the dispersion of one of the media laterally in momentum space (Fig. 1C). Such a shift is analogous to introducing a gauge field and is therefore referred to as a synthetic gauge field. According to theoretical predictions (*11*), when the strength of the synthetic gauge field increases above a certain threshold, refraction can transit from positive to negative. However, this phenomenon has not been observed yet.

Initially started by the research advances in cold atom physics (*13*), synthetic gauge fields have been extensively used to implement topological phases in classical wave systems, including in the emerging fields of topological photonics (*14*–*16*) and topological acoustics (*17*). Previous studies have shown how a synthetic gauge field, $\mathbf{A}$, can generate an effective magnetic field $\mathbf{B} = \nabla \times \mathbf{A}$ and hence induce various phenomena associated with nontrivial band topology. Such phenomena can be regarded as originating from the presence of the effective $\mathbf{B}$ fields, rather than the underlying $\mathbf{A}$ fields (*18*–*32*). However, recent studies have shown that synthetic gauge fields can themselves be a powerful tool for wave manipulation even if the associated magnetic field vanishes ($\nabla \times \mathbf{A} = 0$), such as in the case where $\mathbf{A}$ is spatially uniform (*11*, *12*, *33*, *34*). Here, we shall experimentally demonstrate the use of curl-free and uniform synthetic gauge fields to implement negative refraction.

There are two approaches to constructing uniform synthetic gauge fields. The first is through dynamical modulation on a photonic lattice or metamaterial (*11*, *12*, *20*, *35*). In particular, it is known that modulated two-dimensional (2D) lattices can be effectively realized, without resorting to actual time-dependent modulation, by using 3D waveguide arrays in which the axial spatial direction plays the role of time (*21*, *33*). The second approach is to use media that are moving relative to each other; the light-dragging effect, or relativistic Fresnel drag effect, can shift isofrequency dispersion contours in momentum space (*36*–*38*). So far, neither approach has been used to demonstrate negative refraction.

Here, we adopt an alternative approach to implement the dispersion-shifting effect of a synthetic gauge field and thereby achieve gauge

[1]Interdisciplinary Center for Quantum Information, State Key Laboratory of Modern Optical Instrumentation, ZJU-Hangzhou Global Science and Technology Innovation Center, Zhejiang University, Hangzhou 310027, China. [2]Division of Physics and Applied Physics, School of Physical and Mathematical Sciences, Nanyang Technological University, 21 Nanyang Link, Singapore 637371, Singapore. [3]Centre for Disruptive Photonic Technologies, The Photonics Institute, Nanyang Technological University, 50 Nanyang Avenue, Singapore 639798, Singapore. [4]Research Center of Fluid Machinery Engineering and Technology, School of Physics and Electronic Engineering, Jiangsu University, Zhenjiang 212013, China.
*Corresponding author. Email: jsdxshx@ujs.edu.cn (H.-x.S.); yidong@ntu.edu.sg (Y.C.); blzhang@ntu.edu.sg (B.Z.)
†These authors contributed equally to this work.

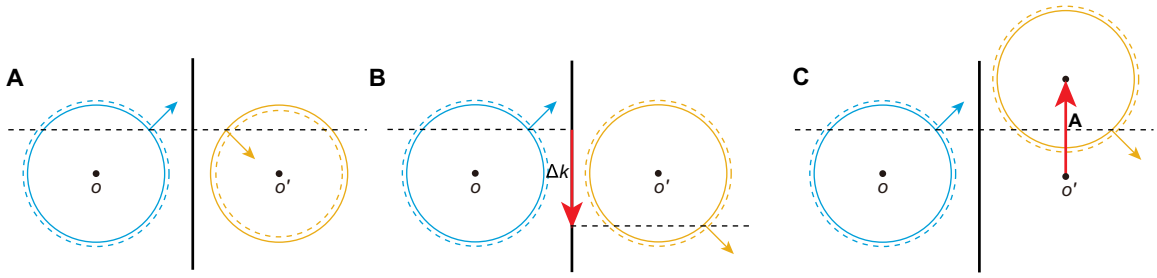

Fig. 1. Mechanisms of negative refraction. A beam is incident from left to right onto the interface between two media. Solid and dashed lines represent the isofrequency dispersion contours at the operating frequency and at a slightly higher frequency, respectively. *O* and *O*′ are the origins in momentum space. (**A**) Negative refraction induced by a bulk negative refractive index in the right medium. (**B**) Negative refraction induced by phase discontinuities in a metasurface, where Δ*k* represents the additional momentum provided along the interface. (**C**) Negative refraction induced by a synthetic gauge field in (**A**) that shifts the dispersion contours in the right medium laterally.

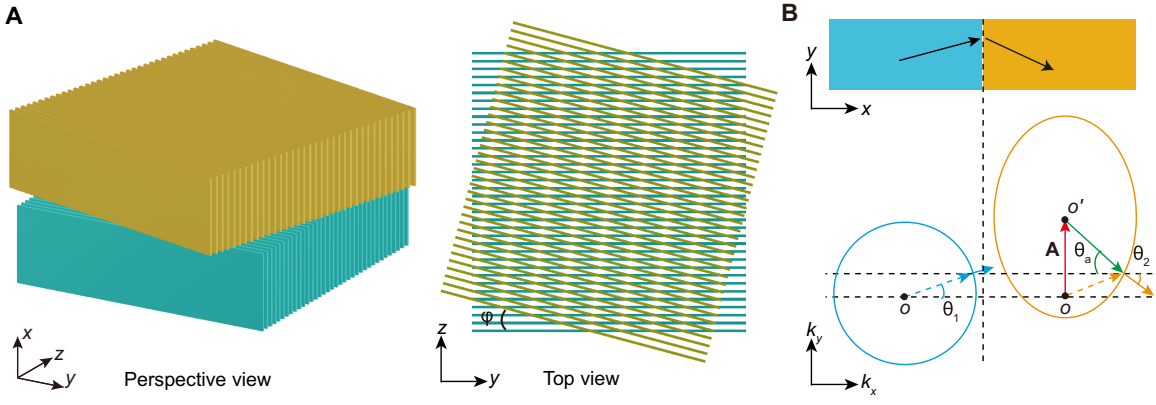

Fig. 2. Implementation of effective gauge field in a twisted bilayer acoustic metamaterial. (**A**) Perspective and top views of the acoustic metamaterial. The bottom (blue) and top (orange) layers are stacked with hard solid plates in the air (the background medium). The top layer is twisted around the *x* axis by φ, forming a Moiré pattern interface with the bottom layer. (**B**) Synthetic gauge fields and negative refraction in the twisted bilayer acoustic metamaterial. For a fixed k_z, the gauge fields for the bottom and top layers are 0 and $\mathbf{A} = \tan(\varphi)k_z\hat{y}$, respectively. The blue dashed (solid) arrow denotes the wave vector (group velocity) of the incident beam. The orange dashed (solid) arrow denotes the wave vector (group velocity) of the refracted beam. θ_1, θ_a, and θ_2 are the incidence angle, the angle of the local wave vector in the gauge-field medium, and the refraction angle, respectively. The red and green arrows represent the gauge field and the local wave vector of the refracted beam, respectively.

field–induced negative refraction. We then exploit this to demonstrate the phenomenon of waveguiding via backward-propagating modes. Our experiments are carried out in twisted bilayer and trilayer acoustic metamaterials, whose gauge fields in the *xy* plane are effectively parameterized by the choice of wave number along the third spatial axis. This design provides a way to construct synthetic gauge fields without relying on dynamical modulation or relative motion.

RESULTS

The design of the twisted bilayer acoustic metamaterial is shown in Fig. 2A. The bottom and top layers are 3D structures consisting of alternating hard solid plates of thickness $w = 3$ mm separated by air gaps of thickness $w_b = 4.1$ mm. Because of the deeply subwavelength features, the two layers can be treated as a continuous effective medium. The top layer is rotated around the *x* axis by an angle of φ. By selecting a fixed k_z, the 3D geometry can be reduced to a 2D geometry in the *xy* plane. The isofrequency contour for the bottom layer is a 2D circle of radius k_0 (where k_0 is the wave vector in the air) centered at the origin of momentum space, as shown in Fig. 2B. The corresponding effective refractive index is $n_1 = 1$. The isofrequency contour for the top layer is an ellipse with major axis $k_0/\sin(\varphi)$ and minor axis k_0, meaning that the *x* (*y*) component of the corresponding effective refractive index is $n_x = 1$ [$n_y = 1/\sin(\varphi)$]. When adjusting the value of k_z, the isofrequency contour for the bottom layer stays intact, but the isofrequency contour for the top layer, although maintaining its shape, is shifted by $A_y = \tan(\varphi)k_z$ in the k_y direction. By selecting the value of k_z, we can obtain an effective gauge potential $\mathbf{A} = A_y\hat{y}$ in the reduced 2D system. Because the third dimension (*z* axis) is reserved for the construction of synthetic gauge fields, we will look at the wave dynamics only in the projected *xy* plane. More details of the metamaterial design can be found in the Supplementary Materials.

In the reduced 2D system, when an acoustic wave is incident from the bottom layer (henceforth called the "normal medium") to the top layer (henceforth called the "gauge-field medium" due to the nonzero effective gauge potential at a fixed k_z), as shown in Fig. 2B, refraction is governed by a modified Snell's law involving the gauge field

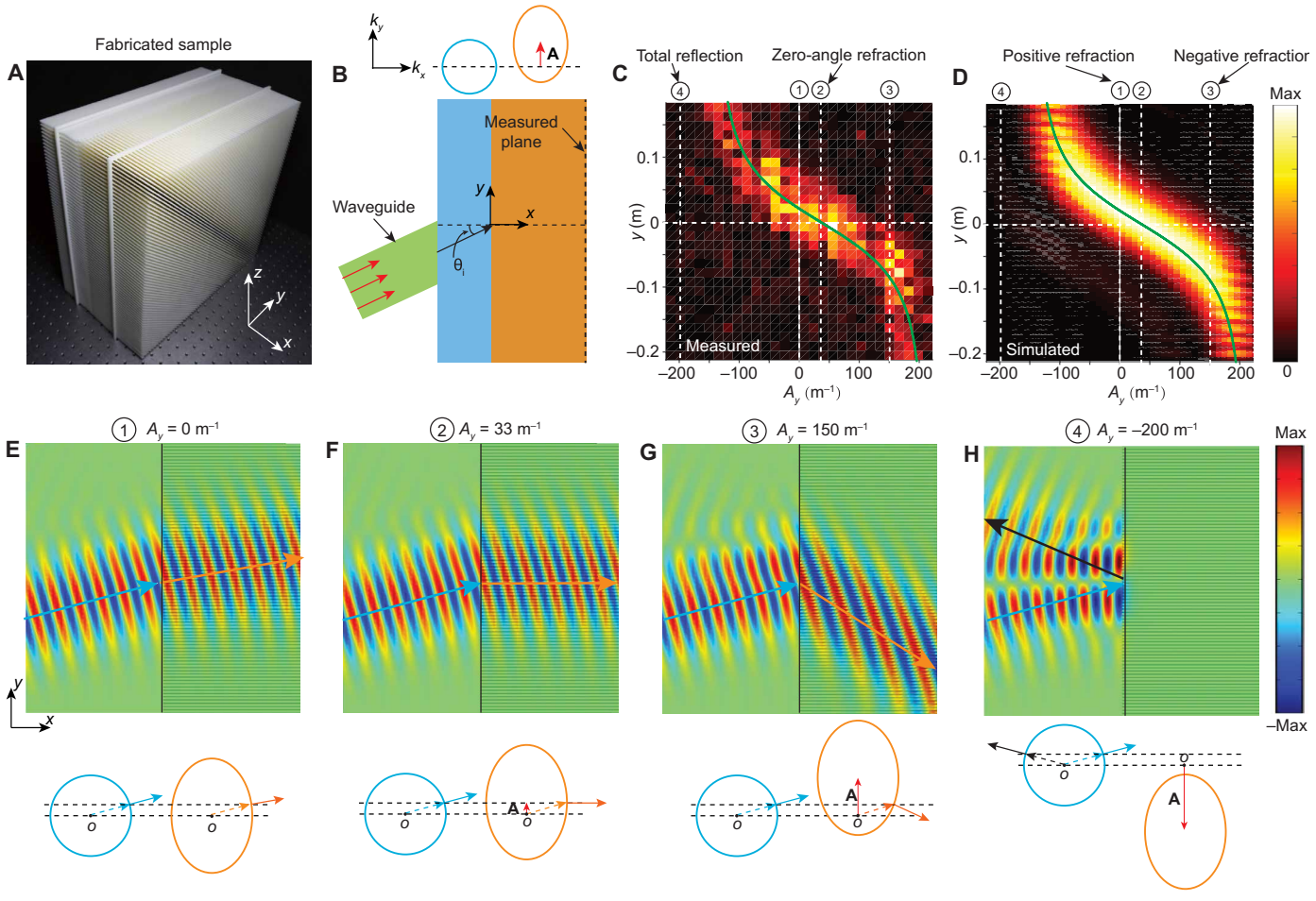

Fig. 3. Transition between positive and negative refraction with varying gauge-field strength. (**A**) Photograph of the fabricated sample. (**B**) Top view of the experimental setup. The width of the gauge-field medium is 140 mm. The acoustic field distributions are measured on the sample's right surface at 7 kHz. The acoustic wave is coupled into the sample via a rectangular waveguide. The incidence angle of the acoustic beam from the waveguide is $\theta_a = 15°$. (**C** and **D**) Measured and simulated acoustic energy distributions at the right surface of the sample for different gauge-field strengths. The green line represents the analytical solution for the beam center in the measured plane. The color bar indicates the energy intensity. (**E** to **H**) Simulated acoustic field distributions under different gauge field potentials **A**. The plotted range for each figure is [–200 mm, 200 mm]^2. The color bar indicates the acoustic pressure. The bottom panels show momentum-space diagrams with dashed (solid) arrows denoting the wave vector (group velocity).

$$\sin(\theta_1)\, n_1 = \sin(\theta_a)\, n_2 + A_y/k_0 \quad (1)$$

$$\theta_2 = \arctan\left[\tan(\theta_a)\, n_x^2/n_y^2\right] \quad (2)$$

with

$$n_2 = n_x n_y / \sqrt{[n_y \cos(\theta_a)]^2 + [n_x \sin(\theta_a)]^2} \quad (3)$$

Here, θ_1 and θ_2 are the angles of incidence and refraction, respectively; n_2 is an effective refractive index in the gauge-field medium; and θ_a is the angle of the local wave vector in the gauge-field medium (the green arrow in Fig. 2B). Note that the gauge-field medium is slightly anisotropic, but anisotropy alone does not cause negative refraction. Equation 1 is obtained from the continuity boundary condition, whereas Eq. 2 describes the relationship between the local wave vector and the group velocity in the anisotropic gauge-field medium. Equation 3 indicates that the effective refractive index n_2 varies with θ_a, owing to the anisotropy of the gauge-field medium. One can see that θ_a and θ_2 have the same sign and $\theta_a = \theta_2$, when $n_x = n_y$ (i.e., the gauge-field medium becomes isotropic).

We now proceed to demonstrate gauge field–induced negative refraction. The fabricated sample with $\varphi = 45°$ is shown in Fig. 3A. Acoustic waves are coupled into the sample via a rectangular waveguide with a narrow width in the z direction, as shown in Fig. 3B and fig. S3. The width along z is so narrow that the input can be treated as a delta function in z, whose Fourier transform covers almost all k_z components. In the xy plane, the waveguide launches an acoustic beam into the normal medium with incidence angle $\theta_i = 15°$. We set the coordinate system such that the origin lies at the crossing point between the waveguide axis and the Moiré pattern interface. We then map the output field pattern along the right surface (see fig. S2). By locating the center of the output beam, we determine the angle of refraction. By extracting different k_z components, we obtain results for different gauge fields, as shown in Fig. 3C. As the gauge-field strength varies, the angle of refraction evolves from positive ($A_y = 0$ m^{-1}; see Fig. 3E) to zero ($A_y = 33$ m^{-1};

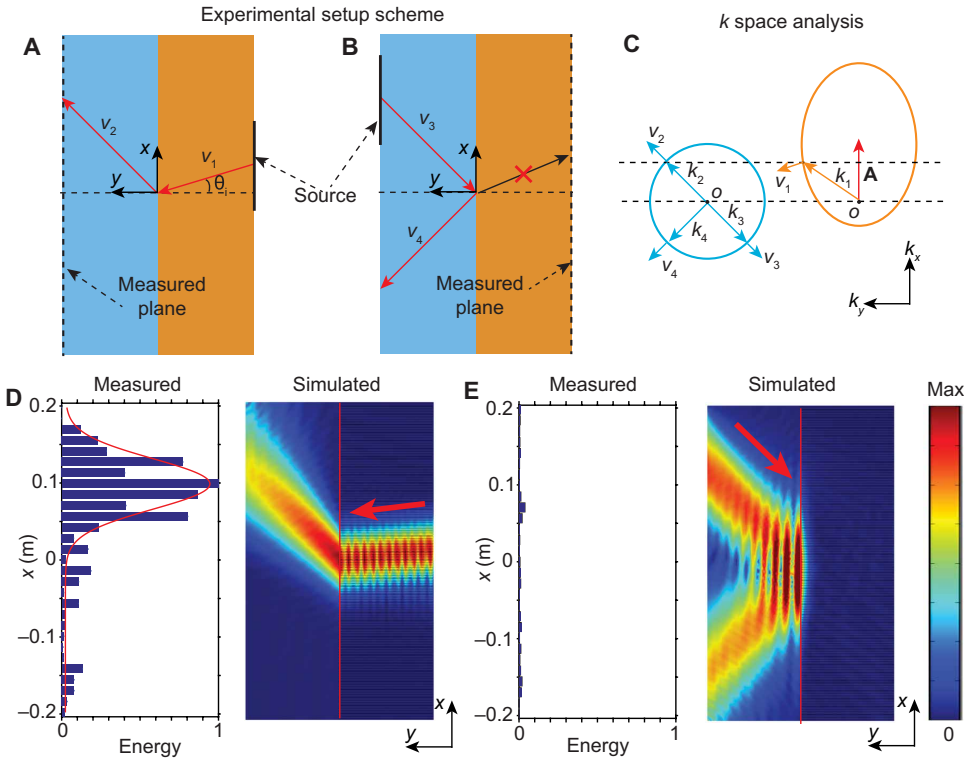

Fig. 4. Observation of nonreciprocal negative refraction and one-way mirror. (**A** and **B**) Top views of the experimental setup for different incident beams. The widths of the gauge-field medium (orange) and the normal medium (blue) are 120 mm. The field distributions at 8 kHz are measured along the sample's left (right) surface for incidence from the right (left) side. The incident angle θ_i is 6.6°. (**C**) Momentum-space analysis. k_1 (k_2) and v_1 (v_2) are the incident (refracted) momentum and group velocity of the beam. k_3 and v_3 are the time-reversed counterparts of the refracted beam associated with k_2. k_4 and v_4 are the reflected momentum and group velocity corresponding to the incident beam with k_3. (**D** and **E**) Left: Normalized measured energy with $A_y = 137\ m^{-1}$ along the measurement plane indicated in (A) and (B). The red curve in the left inset of (D) is the fitted Gaussian profile of the measured energy distribution. Right: Simulated field distributions, with colors representing the acoustic pressure amplitude.

see Fig. 3F) and then to negative values ($A_y = 150\ m^{-1}$; see Fig. 3G). The threshold value of A_y (at which the refraction angle is zero) corresponds to the k_y value of the incident wave. Beyond the threshold, the incident wave couples to the lower branch of the isofrequency contour of the gauge-field medium, resulting in negative refraction. On the basis of Eqs. 1 to 3, we obtain the analytical solutions of the beam center positions at the measured plane, as shown by the green lines in Fig. 3 (C and D). The measured, simulated, and analytical results are in excellent agreement.

The gauge fields effectively break time-reversal (T) symmetry, rendering the in-plane beam propagation nonreciprocal (*11*). It should be noted that the 3D acoustic metamaterial as a whole is T-symmetric, but in the reduced 2D system, for each specified nonzero k_z, T can be effectively broken. This is similar to how a T-symmetric Weyl semimetal can be projected into 2D by taking a fixed wave vector, whereupon it is described by a 2D Chern insulator with broken T (*26*, *39*, *40*).

To explicitly demonstrate this effective T-breaking, we set up the experiment shown in Fig. 4. An acoustic beam is incident from the gauge-field medium to the normal medium, with incidence angle $\theta_i = 6.6°$. The field pattern on the left surface at frequency 8 kHz is measured. Extracting the component with $A_y = 137\ m^{-1}$ (left column of Fig. 4D), we find that the refracted beam center lies at around 0.1 m, indicating negative refraction. This measurement result is consistent with the simulated field pattern (right panel of Fig. 4D). Next, we reverse the refraction beam and measure the field pattern along the right surface, as shown in Fig. 4B. Extracting the component with $A_y = 137\ m^{-1}$, we observe total internal reflection, as shown in Fig. 4E. Hence, the interface between the normal and gauge-field media effectively acts as a one-way mirror. Both the negative refraction and one-way mirror can be explained from momentum-space analysis, as shown in Fig. 4C.

The existence of total internal reflection can be further exploited to perform waveguiding, as demonstrated recently in the context of a photonic lattice (*33*). However, the synthetic gauge field can produce richer physics than what has previously been explored. For example, similar to the transition from positive to negative refraction, we can force the waveguide modes to undergo a transition between forward propagation (i.e., phase and energy propagating in the same direction) and backward propagation (i.e., phase and energy propagating in opposite directions) (*12*).

To accomplish this, we fabricated the twisted trilayer structure shown in Fig. 5A. At a fixed k_z, the cladding and core layers have gauge fields of 0 and $\mathbf{A} = \tan(45°)\ k_z\hat{y}$, respectively, as shown in Fig. 5B. A broadband loudspeaker is placed at the center of the core layer to excite the guided modes. The field distributions in the *yz* plane close to the Moiré pattern interface are mapped out (see the Supplementary Materials for details). Applying the Fourier transform to

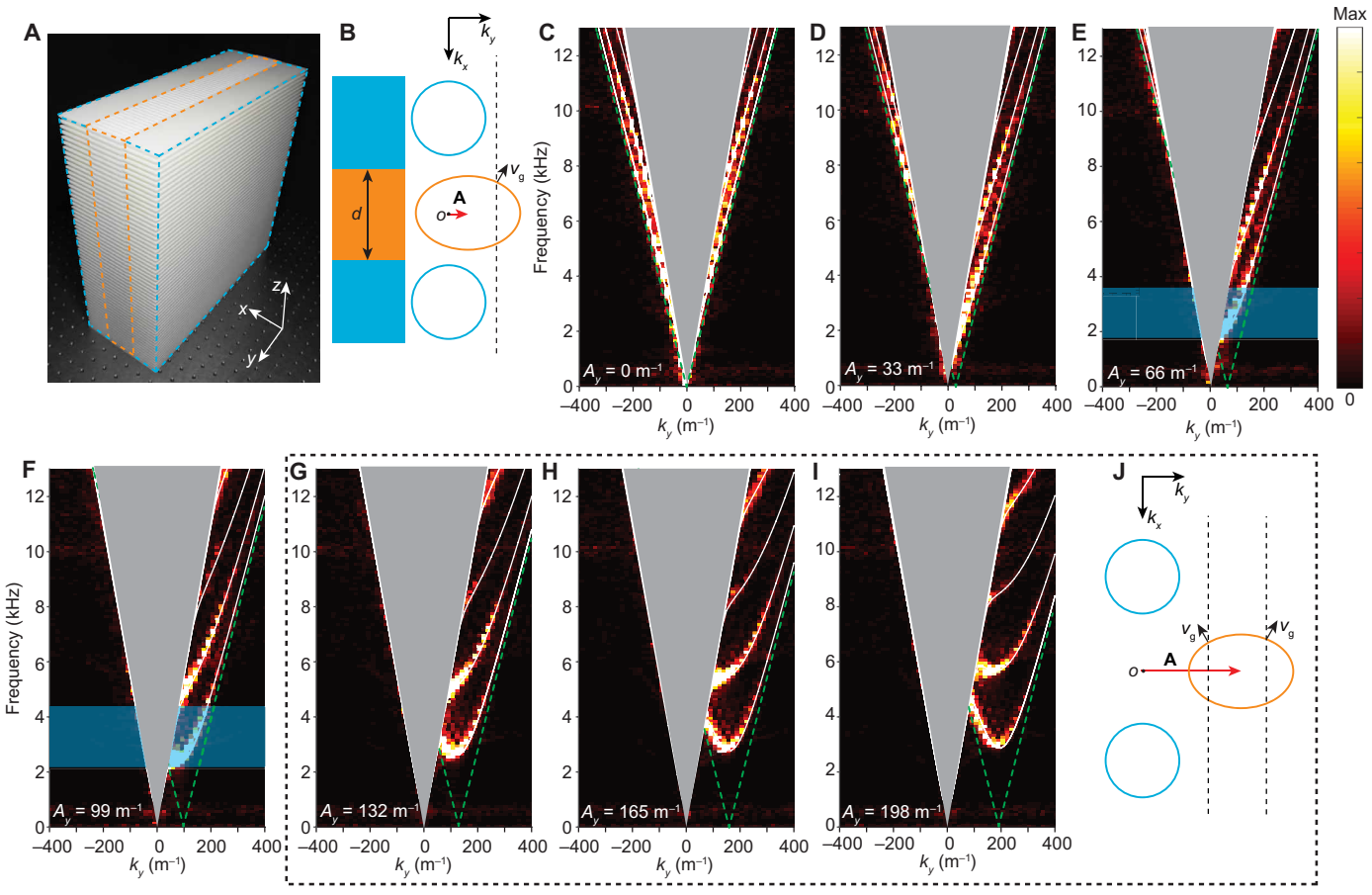

Fig. 5. Experimental demonstration of acoustic gauge-field waveguides with backward-propagating modes. (**A**) Photograph of the experimental sample, consisting of a twisted trilayer structure. The blue and orange regions denote the layers without rotation and with rotation $\varphi = 45°$, respectively. The thickness of the middle layer is $d = 50$ mm. (**B**) Momentum-space analysis for small gauge fields, for which only guided modes with $v_g > 0$ exist. (**C** to **I**) Measured dispersion of the gauge-field waveguides for different effective gauge-field strengths. The color map represents the measured dispersion relation. The color bar at the right of (E) represents the energy intensity. The white lines are the numerically calculated dispersion curves. The green dashed lines and the gray regions represent the light cones for the core and cladding, respectively. The blue highlights indicate the region of single-mode one-way waveguiding. (**J**) Momentum-space analysis for large gauge fields, corresponding to the cases (G to I) for which there exist guided modes with $v_g > 0$ and $v_g < 0$.

the measured field distributions, we obtain the dispersion curves in the k_y-k_z momentum space over a range of frequencies. For a fixed gauge-field strength (corresponding to a fixed k_z), the dispersion can be plotted as a function of k_y and frequency. Thus, we experimentally characterize a class of acoustic gauge-field waveguides with different gauge-field strengths, as shown in Fig. 5 (C to I). For comparison, numerically simulated dispersions of the guided modes are plotted as white lines. The corresponding analytical calculations, based on the continuum theory, are shown in fig. S3.

As shown in Fig. 5C, in the absence of gauge fields, the guided modes emerging from the light cone are symmetric around $k_y = 0$ (these guided modes can exist because the light cone in the core is slightly larger than that in cladding layers). In the presence of gauge fields, as shown in Fig. 5 (D to I), we observe the following four notable features of gauge field–induced waveguiding (*12*): (i) The dispersion curves of the guided modes are asymmetric around $k_y = 0$, indicating effective nonreciprocity. (ii) The fundamental mode acquires a nonzero cutoff frequency. This is unlike conventional waveguides, where the fundamental dispersion curves generally start from zero frequency (*12*), as in Fig. 5C. (iii) In certain frequency ranges, only a single unidirectional mode exists, for example, in the blue-highlighted regions in Fig. 5 (E and F). Single-mode one-way waveguiding is known to arise from the bulk band topology of Chern insulators (or their classical wave analogs) (*17*–*19*), but in this case, the phenomenon arises in the context of a simple gauge-field configuration without complicated band structure effects. (iv) Backward-propagating modes with negative group velocities ($\partial f/\partial k_y < 0$), as shown in Fig. 5 (G to I). From the momentum-space diagrams of Fig. 5 (B and J), we can see that these backward-propagating modes emerge once the gauge-field strength crosses a certain threshold value.

DISCUSSION

We have thus experimentally demonstrated negative refraction induced by synthetic gauge fields. The designed twisted bilayer acoustic metamaterial is ideal for this demonstration owing to having a straightforward continuum description and continuous tunability of the synthetic gauge fields via the choice of out-of-plane wave number. Synthetic gauge fields are a promising way to produce a

range of interesting wave phenomena, distinct from previous approaches based on negative bulk refractive indices or surface phase discontinuities. We have demonstrated the use of gauge fields to create waveguides in which backward propagation characteristics emerge beyond a certain threshold gauge-field strength. With the introduction of nonuniform gauge fields, we envision that many other novel concepts of devices including the flat lens can be achieved. Similar design principles should be applicable to achieve gauge field–induced manipulation of light and elastic waves.

MATERIALS AND METHODS

Experiment method

All samples are fabricated using the additive manufacturing technique. The material is a photosensitive resin with a density of 1.10 g cm^{-3} and a modulus of 2880 MPa. The acoustic signals are recorded with the Brüel & Kjær 3160-A-022 module and analyzed with a commercial software PULSE. In the measurement of the triple-layer twisted structure, the sound signal is launched by a balanced armature speaker (radius of 1 mm) that is driven by a power amplifier. The sound is then guided to the sample center via a narrow tube (radius of 1.5 mm and length of 200 mm). The probe and reference microphones (radius of 3.2 mm; Brüel & Kjær Type 4961) are separately placed in a sealed sleeve with a long tube (radius of 1 mm and length of 100 mm). The tube connecting to a probe microphone is inserted into the sample to detect the acoustic wave at the Moiré pattern interface point by point. The position of the reference microphone is fixed around the sound source to detect the reference signal. The scanning region takes up an area of about 400 mm by 400 mm, and the resolution is around 7.07 mm by 7.07 mm. The experimental setup of the bilayer twisted structure is similar to that of the triple-layer structure, except that the acoustic signal is guided to the sample via a rectangular waveguide with a width of 10 cm and a height of 1 cm. The measured planes are marked in Figs. 3B and 4 (A and B).

Simulation method

We use the acoustic module of commercial software COMSOL Multiphysics 5.0 to calculate the dispersions of the guided modes and acoustic field patterns. In our simulations, the surfaces of the photosensitive resin are set as hard boundaries. The background fluid is air with a density of 1.18 kg m^{-3}, and the speed of airborne sound is 343 m s^{-1}. To calculate the dispersions of the acoustic gauge-field waveguides, periodic boundary conditions are applied to the y and z directions. To simulate the field patterns in Figs. 2 and 3, periodic boundaries are applied to the z direction and scattering boundaries are applied to the x and y directions.

SUPPLEMENTARY MATERIALS

Supplementary material for this article is available at https://science.org/doi/10.1126/sciadv.abj2062

REFERENCES AND NOTES

1. V. G. Veselago, The electrodynamics of substances with simultaneously negative values of ε and μ. *Usp. Fiz. Nauk* **92**, 517 (1967).
2. J. B. Pendry, Negative refraction makes a perfect lens. *Phys. Rev. Lett.* **85**, 3966–3969 (2000).
3. R. A. Shelby, D. R. Smith, S. Schultz, Experimental verification of a negative index of refraction. *Science* **292**, 77–79 (2001).
4. D. R. Smith, J. B. Pendry, M. C. Wiltshire, Metamaterials and negative refractive index. *Science* **305**, 788–792 (2004).
5. H. J. Lezec, J. A. Dionne, H. A. Atwater, Negative refraction at visible frequencies. *Science* **316**, 430–432 (2007).
6. N. Yu, P. Genevet, M. A. Kats, F. Aieta, J. P. Tetienne, F. Capasso, Z. Gaburro, Light propagation with phase discontinuities: Generalized laws of reflection and refraction. *Science* **334**, 333–337 (2011).
7. J. B. Pendry, A chiral route to negative refraction. *Science* **306**, 1353–1355 (2004).
8. J. Valentine, S. Zhang, T. Zentgraf, E. Ulin-Avila, D. A. Genov, G. Bartal, X. Zhang, Three-dimensional optical metamaterial with a negative refractive index. *Nature* **455**, 376–379 (2008).
9. N. Yu, F. Capasso, Flat optics with designer metasurfaces. *Nat. Mater.* **13**, 139–150 (2014).
10. M. Khorasaninejad, W. T. Chen, R. C. Devlin, J. Oh, A. Y. Zhu, F. Capasso, Metalenses at visible wavelengths: Diffraction-limited focusing and subwavelength resolution imaging. *Science* **352**, 1190–1194 (2016).
11. K. Fang, S. Fan, Controlling the flow of light using the inhomogeneous effective gauge field that emerges from dynamic modulation. *Phys. Rev. Lett.* **111**, 203901 (2013).
12. Q. Lin, S. Fan, Light guiding by effective gauge field for photons. *Phys. Rev. X* **4**, 031031 (2014).
13. N. R. Cooper, J. Dalibard, I. B. Spielman, Topological bands for ultracold atoms. *Rev. Mod. Phys.* **91**, 015005 (2019).
14. L. Lu, J. D. Joannopoulos, M. Soljačić, Topological photonics. *Nat. Photonics* **8**, 821–829 (2014).
15. A. B. Khanikaev, G. Shvets, Two-dimensional topological photonics. *Nat. Photonics* **11**, 763–773 (2017).
16. T. Ozawa, H. M. Price, A. Amo, N. Goldman, M. Hafezi, L. Lu, M. C. Rechtsman, D. Schuster, J. Simon, O. Zilberberg, I. Carusotto, Topological photonics. *Rev. Mod. Phys.* **91**, 015006 (2019).
17. Z. Yang, F. Gao, X. Shi, X. Lin, Z. Gao, Y. Chong, B. Zhang, Topological acoustics. *Phys. Rev. Lett.* **114**, 114301 (2015).
18. F. D. M. Haldane, S. Raghu, Possible realization of directional optical waveguides in photonic crystals with broken time-reversal symmetry. *Phys. Rev. Lett.* **100**, 013904 (2008).
19. Z. Wang, Y. Chong, J. D. Joannopoulos, M. Soljacic, Observation of unidirectional backscattering-immune topological electromagnetic states. *Nature* **461**, 772–775 (2009).
20. K. Fang, Z. Yu, S. Fan, Realizing effective magnetic field for photons by controlling the phase of dynamic modulation. *Nat. Photonics* **6**, 782–787 (2012).
21. M. C. Rechtsman, J. M. Zeuner, Y. Plotnik, Y. Lumer, D. Podolsky, F. Dreisow, S. Nolte, M. Segev, A. Szameit, Photonic Floquet topological insulators. *Nature* **496**, 196–200 (2013).
22. M. Hafezi, S. Mittal, J. Fan, A. Migdall, J. M. Taylor, Imaging topological edge states in silicon photonics. *Nat. Photonics* **7**, 1001–1005 (2013).
23. A. B. Khanikaev, S. Hossein Mousavi, W. K. Tse, M. Kargarian, A. H. MacDonald, G. Shvets, Photonic topological insulators. *Nat. Mater.* **12**, 233–239 (2013).
24. M. C. Rechtsman, J. M. Zeuner, A. Tünnermann, S. Nolte, M. Segev, A. Szameit, Strain-induced pseudomagnetic field and photonic Landau levels in dielectric structures. *Nat. Photonics* **7**, 153–158 (2013).
25. X. Cheng, C. Jouvaud, X. Ni, S. H. Mousavi, A. Z. Genack, A. B. Khanikaev, Robust reconfigurable electromagnetic pathways within a photonic topological insulator. *Nat. Mater.* **15**, 542–548 (2016).
26. M. Xiao, W.-J. Chen, W.-Y. He, C. T. Chan, Synthetic gauge flux and Weyl points in acoustic systems. *Nat. Phys.* **11**, 920–924 (2015).
27. C. He, X. Ni, H. Ge, X. C. Sun, Y. B. Chen, M. H. Lu, X. P. Liu, Y. F. Chen, Acoustic topological insulator and robust one-way sound transport. *Nat. Phys.* **12**, 1124–1129 (2016).
28. H. Abbaszadeh, A. Souslov, J. Paulose, H. Schomerus, V. Vitelli, Sonic Landau levels and synthetic gauge fields in mechanical metamaterials. *Phys. Rev. Lett.* **119**, 195502 (2017).
29. Z. Yang, F. Gao, Y. Yang, B. Zhang, Strain-induced gauge field and Landau levels in acoustic structures. *Phys. Rev. Lett.* **118**, 194301 (2017).
30. C. Brendel, V. Peano, O. J. Painter, F. Marquardt, Pseudomagnetic fields for sound at the nanoscale. *Proc. Natl. Acad. Sci. U.S.A.* **114**, E3390–E3395 (2017).
31. H. Jia, R. Zhang, W. Gao, Q. Guo, B. Yang, J. Hu, Y. Bi, Y. Xiang, C. Liu, S. Zhang, Observation of chiral zero mode in inhomogeneous three-dimensional Weyl metamaterials. *Science* **363**, 148–151 (2019).
32. Y. Yang, Z. Gao, H. Xue, L. Zhang, M. He, Z. Yang, R. Singh, Y. Chong, B. Zhang, H. Chen, Realization of a three-dimensional photonic topological insulator. *Nature* **565**, 622–626 (2019).
33. Y. Lumer, M. A. Bandres, M. Heinrich, L. J. Maczewsky, H. Herzig-Sheinfux, A. Szameit, M. Segev, Light guiding by artificial gauge fields. *Nat. Photonics* **13**, 339–345 (2019).
34. M.-I. Cohen, C. Jörg, Y. Lumer, Y. Plotnik, E. H. Waller, J. Schulz, G. von Freymann, M. Segev, Generalized laws of refraction and reflection at interfaces between different photonic artificial gauge fields. *Light Sci. Appl.* **9**, 200 (2020).
35. K. Fang, Z. Yu, S. Fan, Photonic Aharonov-Bohm effect based on dynamic modulation. *Phys. Rev. Lett.* **108**, 153901 (2012).
36. T. M. Grzegorczyk, J. A. Kong, Electrodynamics of moving media inducing positive and negative refraction. *Phys. Rev. B* **74**, 033102 (2006).
37. D. Correas-Serrano, J. S. Gomez-Diaz, Nonreciprocal and collimated surface plasmons in drift-biased graphene metasurfaces. *Phys. Rev. B* **100**, 081410 (2019).
38. P. A. Huidobro, E. Galiffi, S. Guenneau, R. V. Craster, J. B. Pendry, Fresnel drag in space–time-modulated metamaterials. *Proc. Natl. Acad. Sci. U.S.A.* **116**, 24943–24948 (2019).

39. N. P. Armitage, E. J. Mele, A. Vishwanath, Weyl and Dirac semimetals in three-dimensional solids. *Rev. Mod. Phys.* **90**, 015001 (2018).
40. L. Lu, L. Fu, J. D. Joannopoulos, M. Soljačić, Weyl points and line nodes in gyroid photonic crystals. *Nat. Photonics* **7**, 294–299 (2013).

Acknowledgments
Funding: This work is funded by Singapore Ministry of Education grants MOE2016-T3-1-006 and MOE2019-T2-2-085; National Natural Science Foundation of China grants 62175215, 11774137, 12174159, and 51779107; and State Key Laboratory of Acoustics, Chinese Academy of Science grant SKLA202016. **Author contributions:** Y.Y. created the design and performed the simulations. Y.Y., R.L., and X.L. did the theoretical analysis. Y.Y., Y.G., and H.-x.S. fabricated the sample and designed the experiments. H.-x.S., Y.G., Y.-j.G., and D.J. performed measurements. Y.Y., R.L., S.-q.Y., Y.C., and B.Z. analyzed data and wrote the paper. Y.C. and B.Z. supervised the project. All authors contributed extensively to this work. **Competing interests:** The authors declare that they have no competing interests. **Data and materials availability:** All data needed to evaluate the conclusions in the paper are present in the paper and/or the Supplementary Materials. Raw experimental data are available from the Digital Repository of Nanyang Technological University (DR-NTU) at https://doi.org/10.21979/N9/T6YXVC.

Submitted 28 April 2021
Accepted 21 October 2021
Published 8 December 2021
10.1126/sciadv.abj2062

ScienceAdvances

Demonstration of negative refraction induced by synthetic gauge fields

Yihao YangYong GeRujiang LiXiao LinDing JiaYi-jun GuanShou-qi YuanHong-xiang SunYidong ChongBaile Zhang

Sci. Adv., 7 (50), eabj2062. • DOI: 10.1126/sciadv.abj2062

Science Advances (ISSN) is published by the American Association for the Advancement of Science. 1200 New York Avenue NW, Washington, DC 20005. The title *Science Advances* is a registered trademark of AAAS.